J. Zhang, J.D. Biggs, D. Ye, Z. Sun
Extended-State-observer Based Event-Triggered Orbit-Attitude Tracking for Low-Thrust Spacecraft
IEEE Transactions on Aerospace and Electronic Systems
In press - Published online 22/11/2019
doi:10.1109/TAES.2019.2955257

Extended-state-observer based event-triggered orbit-attitude tracking for low-thrust spacecraft

Jianqiao Zhang, James Douglas Biggs, Dong Ye, and Zhaowei Sun

Abstract

This paper addresses the coupled orbit-attitude tracking problem using low-thrust propulsion while aiming to minimize on-board spacecraft system communication. An adaptive controller is proposed by employing an event-triggered control and an extended-state-observer, where a simple strategy to tune the observer parameters is provided. Moreover, the event-triggering strategy updates and allocates the control signal to the thrusters at prescribed discrete events and is shown to significantly reduce the data-rate requirement. Finally, the performance of the controller is illustrated through numerical examples.

Index Terms

Coupled orbit-attitude tracking; low-thrust propulsion; minimize on-board communication; event-triggered control; extended-state-observer.

I. Introduction

Relative orbit-attitude tracking control is a key enabling technology for spacecraft formation flying, spacecraft rendezvous and docking, high accuracy on-orbit monitoring, and asteroid hovering [1]–[4]. Moreover, NASA and the US National Research Council have identified relative guidance and control algorithms as one of the high-priority enabling technologies for the next generation of distributed space systems [5]. The potential adaptability of formation flying spacecraft to changing mission goals have created new opportunities for scientific and commercial applications. However, the precision control, measurement and modeling challenges of spacecraft formation flying have rendered some missions too costly.

Recent advances in small spacecraft and low-thrust propulsion technology mean that such missions are becoming more attractive with the potential to progress the Technology Readiness Level. In addition to having high specific impulse [6], the use of low-thrust, continuous, propulsion enables the implementation of advanced control techniques for high tracking accuracy not possible with chemical propulsion [7]. Moreover, these propulsion systems can provide a magnitude ranging from μN to N and specific impulse ranging from 10^1s to 10^3s, which could potentially be used for, high-precision, relative orbit-attitude motion control of small spacecraft. The use of continuous low-thrust

This work is supported by the China Scholarship Council.

J. Zhang, D. Ye and Z. Sun are with the Research Center of Satellite Technology, Harbin Institute of Technology, Harbin, 150001, P. R. China. (e-mail: zhangjianqiao@hit.edu.cn; yed@hit.edu.cn; sunzhaowei@hit.edu.cn; corresponding author: Jianqiao Zhang.)

J. D. Biggs is with the Department of Aerospace Science and Technology, Politecnico di Milano, Milan, 20156, Italy. (e-mail: jamesdouglas.biggs@polimi.it.)

has been proposed for use in time-optimal transfers from Earth to the Earth-Moon Lagrange point L1 in [8], for orbit transfers generated in restricted N-body problems in [9], and the generation of highly non-Keplerian orbits in [10]. Developing the state-of-the-art in continuous low-thrust applications to relative orbit-attitude control of small spacecraft is the motivation of this paper. This paper develops a control algorithm for the relative orbit-attitude tracking control of small spacecraft using low-thrust propulsion which includes modeling and environmental disturbances and thruster output bias. Critically this includes installation errors of the thrusters, which induce undesirable rotational and translational motions due to the coupled orbit-attitude dynamics.

In the current literature, nonlinear control techniques have been applied to develop tracking controls for spacecraft with coupled orbit-attitude dynamics. For instance, based on a sliding mode control (SMC) technique, a finite-time controller was proposed in [1] to synchronize formation flying spacecraft. A linear sliding mode controller integrated with an artificial potential function method was developed to include collision-avoidance in [3]. In addition, an adaptive finite-time control scheme was proposed in [2] for near asteroid hovering of a rigid spacecraft, and new vision-based attitude control methods were developed in [11] for in-orbit optical tracking of resident space objects. Moreover, other control methods such as proportion-derivative (PD) type adaptive controllers in [4], output feedback controllers without the requirement of relative linear and angular velocity measurements in [12], [13], and adaptive back-stepping controller in [14], have been employed to address tracking problems of six-degrees-of-freedom (6-DOF) spacecraft proximity operations.

Control design that compensates for uncertainties in modeling and disturbances is often treated using back-stepping control or SMC, which requires a known disturbance upper-bound to guarantee stability and enable efficient tuning [14]–[16]. However, in practice the upper bound may be uncertain over a mission lifetime, particularly in the case of anomalies such as faults, thruster mis-firing and shifts in the centre-of-mass due to fuel usage. In contrast, active disturbance rejection control (ADRC) can effectively deal with the disturbance including model uncertainty and external disturbances [17]. The core of ADRC is to regard the disturbance as an extended system state, estimate the state by an extended state observer (ESO), and use the estimated information as feedback state to attenuate the disturbance. ESO does not need any information of the disturbance and has been implemented for spacecraft trajectory tracking to induce asymptotic convergence to the desired state to a small controllable region using a linear ESO in [17]. Nonlinear ESOs have also been developed, which can provide faster convergence and higher accuracy, in [18]–[21]. However, the selection of the tuning parameters of nonlinear ESOs to ensure small tracking errors is a complex problem often involving rigorous experimental tuning [21]. Although a rigorous proof of the stability of the ESO was given in [19], the use of a homogeneous method makes the proof process and the selection of the ESO parameters complicated. In this paper, a finite-time ESO motivated by [19], [20] is developed, and a theoretical basis for gain tuning is obtained through Lyapunov theory. Compared with the ESO in [20], an additional nonlinear term is applied to improve the observer performance close to the origin. Moreover, the ESO proposed in this paper permits a simple switching between linear ESO and nonlinear ESO. For spacecraft proximity operations in low Earth orbit, which require high control performance and are with significant disturbances, a nonlinear ESO is preferred due to its known superior performance compared to linear ESO. However, nonlinear ESOs tend to require more extensive experimental tuning making them more complex to implement. Thus, there is generally a

trade off between performance and implementation complexity.

For on-board spacecraft, the control signal is computed digitally using microprocessors based on the sampled sensor measurements. This signal is then distributed to the actuators via a continuous transmission [22]. If the signal is not necessary to be updated, it will waste the spacecraft's embedded resources [23]. Moreover, the communication bandwidth will be shared by different independent modules which is highly restricted on small spacecraft [24]. Event-triggered control, is a control strategy that can alleviate the communication requirement by the signal to actuators are sent only when a prescribed event-triggering condition is met. This method establishes a link between the sampling period of the controller and the system measurement, to reduce the rate of communication transmission. This is in contrast to traditional fixed-time sampling control methods which may unnecessarily use on-board communication resources [25]. Event-triggered control has been applied to many kinds of nonlinear systems, such as hybrid switched systems in [25], uncertain nonlinear systems in [26], multi-agent systems in [27], [28], and networked singular system in [29]. Relatively few results related to spacecraft control exists, and those that do focus on spacecraft attitude control [22]–[24]. Moreover, most of the design schemes assume that the closed-loop system has input-to-state stability (ISS) with respect to the measurement errors, which is difficult to satisfy in practice [26]. In [26], the ISS assumption on the measurement error of a simple nonlinear system is removed by designing the triggering strategy based on the measurement error of the control signal. However, it is hard to straightforward extend the state-of-the-art in event-triggered control of [26] to spacecraft orbit-attitude control, since a 6-DOF spacecraft dynamical model considering the presence of uncertainties and the complexities of the relative orbit-attitude coupling is highly nonlinear and coupled. This paper combines an event-triggered adaptive SMC with an ESO to achieve high-precision relative tracking control of a 6-DOF spacecraft, without the need for the ISS assumption, and further reduces the signal transmission. Moreover, the application of event-triggered control to 6-DOF spacecraft control is considered here for the first time.

The remainder of this paper is organized as follows. In Sec.II, the relative 6-DOF dynamics are formulated, and some lemmas used for controller stability analysis are presented. The main results are obtained in Sec.III. An event-triggered adaptive SMC with finite-time ESO is proposed to address the spacecraft tracking control problem, and its convergence is proved via Lyapunov stability theorem. Then, a simulation study of a relative orbit-attitude tracking problem for low-thrust micro spacecraft is undertaken in Sec.IV to show the effectiveness of the controller. Finally, some conclusions are given in Sec.V.

II. Spacecraft Modeling and Preliminaries

A chaser spacecraft is modeled as a rigid body operating in the gravitational field of the Earth. The objective is to control the spacecraft's trajectory to a relative pose (position and attitude) with respect to the trajectory of a virtual rigid leader. The relative 6-DOF equations of motions derived from the Special Euclidean group $\mathrm{SE}(3)$ are utilized to describe the relative pose tracking error.

A. Kinematics and Dynamics of a Single Spacecraft

Three coordinate frames are used: the Earth centered inertial frame $\mathscr{F}_I$, the body-fixed frames $\mathscr{F}_b$, and the orbit frame of the leader $\mathscr{F}_o$. $\mathscr{F}_o$ is a right-handed orthogonal coordinate frame, whose origin is located in the mass center of the spacecraft. The *x* axis points in the radial direction from the origin of $\mathscr{F}_I$ to the virtual spacecraft, the *y* axis is in the flight direction and the *z* axis is obtained by using the cross-product. Then, the 6-DOF kinematics and dynamics of a rigid spacecraft can be described by [30]

$$\dot{\boldsymbol{R}} = \boldsymbol{R}\boldsymbol{\omega}^{\times}; \quad \dot{\boldsymbol{r}} = \boldsymbol{R}\boldsymbol{v} \tag{1}$$

$$\boldsymbol{J}\dot{\boldsymbol{\omega}} + \boldsymbol{\omega}^{\times}\boldsymbol{J}\boldsymbol{\omega} = \boldsymbol{M}_{\mathrm{G}} + \boldsymbol{\tau}_{\mathrm{c}} + \boldsymbol{d}_{\tau}; \quad m\dot{\boldsymbol{v}} + m\boldsymbol{\omega}^{\times}\boldsymbol{v} = \boldsymbol{f}_{\mathrm{G}} + \boldsymbol{u}_{\mathrm{c}} + \boldsymbol{d}_{f} \tag{2}$$

where $\boldsymbol{R} \in \mathrm{SO}(3)$ is the direct cosine matrix that describes the relative orientation from $\mathscr{F}_b$ to $\mathscr{F}_I$, with $\mathrm{SO}(3)$ the 3-D Special Orthogonal Group denoted by $\mathrm{SO}(3) = \{\boldsymbol{R} \in \mathbb{R}^{3\times 3} : \boldsymbol{R}^{\mathrm{T}}\boldsymbol{R} = \boldsymbol{I}_3, \det(\boldsymbol{R}) = 1\}$, where $\boldsymbol{I}_n$ denotes a n-by-n identity matrix [31]. $\boldsymbol{r} \in \mathbb{R}^3$ is the spacecraft position expressed in $\mathscr{F}_I$, $\boldsymbol{\omega}$ and $\boldsymbol{v}$ are the angular and translational velocities expressed in $\mathscr{F}_b$, and $(\boldsymbol{x})^{\times}$ represents the skew-symmetric matrix of a vector $\boldsymbol{x} \in \mathbb{R}^3$. $\boldsymbol{J}$ is the moment of inertia matrix and m is the mass of the spacecraft, $\boldsymbol{\tau}_{\mathrm{c}}$ and $\boldsymbol{u}_{\mathrm{c}}$ are the control torque and force, implemented using low-thrust, continuous, propulsion, and $\boldsymbol{d}_{\tau}$ and $\boldsymbol{d}_f$ are the external disturbance torque and force respectively. $\boldsymbol{M}_{\mathrm{G}}$ and $\boldsymbol{f}_{\mathrm{G}}$ are the gravity gradient moment and force, whose expressions are [4]

$$\boldsymbol{M}_{\mathrm{G}} = 3\Big(\frac{\mu}{\|\boldsymbol{r}\|^5}\Big)\Big((\boldsymbol{R}^{\mathrm{T}}\boldsymbol{r})^{\times}\boldsymbol{J}(\boldsymbol{R}^{\mathrm{T}}\boldsymbol{r})\Big)$$

$$\boldsymbol{f}_{\mathrm{G}} = -m\Big(\frac{\mu\boldsymbol{R}^{\mathrm{T}}\boldsymbol{r}}{\|\boldsymbol{r}\|^3} + \frac{3J_2\mu r_e^2\boldsymbol{R}^{\mathrm{T}}}{2\|\boldsymbol{r}\|^5}\big(\boldsymbol{E} - \frac{5r_z^2}{\|\boldsymbol{r}\|^2}\boldsymbol{I}_3\big)\boldsymbol{r}\Big)$$

where the oblateness of the Earth J2 is considered, $\mu = 398600.4\mathrm{km}^3/\mathrm{s}^2$ is the gravitational parameter of the Earth, $||\cdot||$ is the Euclidean norm of a vector, $J_2 = 0.00108263$, $r_e = 6378.14\mathrm{km}$ is the Earth's mean equatorial radius, $\boldsymbol{E} = \mathrm{diag}(1,1,3)$, and r_z is the z-axis component of $\boldsymbol{r}$.

For convenience of the control development demonstration, we use the semi-direct product of $\mathbb{R}^3$ and $\mathrm{SO}(3)$ to obtain the Special Euclidean Group $\mathrm{SE}(3)$, which permits us to express (1) compactly as [3]

$$\dot{\boldsymbol{g}} = \boldsymbol{g}(\boldsymbol{V})^{\vee}, \quad \boldsymbol{g} = \begin{bmatrix} \boldsymbol{R} & \boldsymbol{r} \\ \boldsymbol{0}_{1\times 3} & 1 \end{bmatrix} \in \mathrm{SE}(3) \tag{3}$$

where $\boldsymbol{V} = \begin{bmatrix}\boldsymbol{\omega}^{\mathrm{T}} & \boldsymbol{v}^{\mathrm{T}}\end{bmatrix}^{\mathrm{T}}$, and $\boldsymbol{V}^{\vee}$ is defined by

$$\boldsymbol{V}^{\vee} = \begin{bmatrix} \boldsymbol{\omega}^{\times} & \boldsymbol{v} \\ \boldsymbol{0}_{1\times 3} & 0 \end{bmatrix} \in \mathfrak{se}(3)$$

where $\mathfrak{se}(3)$ is the Lie algebra.

For two elements $(\boldsymbol{\omega}, \boldsymbol{v}), (\boldsymbol{\eta}, \boldsymbol{\psi}) \in \mathfrak{se}(3)$, the linear adjoint representation ad between Lie algebra $\mathfrak{se}(3)$ and Lie group SE(3) and its co-adjoint operator ad^* are defined as $\mathrm{ad}_{(\boldsymbol{\omega},\boldsymbol{v})}(\boldsymbol{\eta}, \boldsymbol{\psi}) = (\boldsymbol{\omega}^{\times}\boldsymbol{\eta}, \boldsymbol{\omega}^{\times}\boldsymbol{\psi} - \boldsymbol{\eta}^{\times}\boldsymbol{v})$ and $\mathrm{ad}^*_{(\boldsymbol{\omega},\boldsymbol{v})}(\boldsymbol{\eta}, \boldsymbol{\psi}) =$

$(\boldsymbol{\eta}^{\times}\boldsymbol{\omega}+\boldsymbol{\psi}^{\times}\boldsymbol{v},\boldsymbol{\psi}^{\times}\boldsymbol{\omega})$ [32]. Moreover, ad^* can also be expressed in a matrix form

$$\mathrm{ad}^*_{\boldsymbol{V}}=\begin{bmatrix}-\boldsymbol{\omega}^{\times} & -\boldsymbol{v}^{\times}\\ \mathbf{0}_{3\times3} & -\boldsymbol{\omega}^{\times}\end{bmatrix}$$

which permits us to express the dynamics (2) compactly as [20]

$$\boldsymbol{\Xi}\dot{\boldsymbol{V}}=\mathrm{ad}^*_{\boldsymbol{V}}\boldsymbol{\Xi}\boldsymbol{V}+\boldsymbol{f}(\boldsymbol{\Xi})+\boldsymbol{\Gamma}_c+\boldsymbol{\Gamma}_d \tag{4}$$

where $\boldsymbol{\Xi}=\mathrm{diag}(\boldsymbol{J},m\boldsymbol{I}_3)$, $\boldsymbol{f}(\boldsymbol{\Xi})=\left[\boldsymbol{M}_G^{\mathrm{T}},\boldsymbol{f}_G^{\mathrm{T}}\right]^{\mathrm{T}}$, $\boldsymbol{\Gamma}_c=\left[\boldsymbol{\tau}_c^{\mathrm{T}},\boldsymbol{u}_c^{\mathrm{T}}\right]^{\mathrm{T}}$, and $\boldsymbol{\Gamma}_d=\left[\boldsymbol{d}_\tau^{\mathrm{T}},\boldsymbol{d}_f^{\mathrm{T}}\right]^{\mathrm{T}}$.

B. Mathematical Model of the Spacecraft Tracking System

Let $\boldsymbol{g}_d$ be the desired configuration of the spacecraft, and $\boldsymbol{g}_a$ be the actual configuration of the spacecraft, and then the tracking error of the spacecraft is

$$\boldsymbol{g}_e=\boldsymbol{g}_d^{-1}\boldsymbol{g}_a=\begin{bmatrix}\boldsymbol{R}_e & \boldsymbol{r}_e\\ \mathbf{0}_{1\times3} & 1\end{bmatrix} \tag{5}$$

which can be expressed by exponential coordinates using the logarithm map:

$$\widetilde{\boldsymbol{\eta}}=\begin{bmatrix}\boldsymbol{\Phi}\\ \boldsymbol{\chi}\end{bmatrix},\quad \mathrm{logm}(\boldsymbol{g}_e)=\begin{bmatrix}\boldsymbol{\Phi}^{\times} & \boldsymbol{\chi}\\ \mathbf{0}_{1\times3} & 0\end{bmatrix} \tag{6}$$

$\widetilde{\boldsymbol{\eta}}\in\mathbb{R}^6$ is composed by two parts: $\boldsymbol{\Phi}$ and $\boldsymbol{\chi}$, where $\boldsymbol{\Phi}\in\mathbb{R}^3$ is obtained by the exponential coordinates of SO(3) and represents the attitude tracking error, and $\boldsymbol{\chi}\in\mathbb{R}^3$ is the position tracking error. They can be calculated by [20]

$$\boldsymbol{\Phi}^{\times}=\begin{cases}\mathbf{0}_{3\times3} & \theta=0\\ \dfrac{\theta}{2\sin\theta}(\boldsymbol{R}_e-\boldsymbol{R}_e^{\mathrm{T}}) & \theta\in(-\pi,\pi),\theta\neq0\end{cases}$$

$$\boldsymbol{\chi}=\boldsymbol{S}^{-1}(\boldsymbol{\Phi})\boldsymbol{r}_e,\quad \boldsymbol{S}(\boldsymbol{\Phi})=\boldsymbol{I}_{3\times3}+\frac{1-\cos\theta}{\theta^2}\boldsymbol{\Phi}^{\times}+\frac{\theta-\sin\theta}{\theta^3}(\boldsymbol{\Phi}^{\times})^2$$

where $\theta=||\boldsymbol{\Phi}||=\arccos(0.5(\mathrm{tr}(\boldsymbol{R}_e)-1))$ represents the principal rotation angle, and $\mathrm{tr}(\cdot)$ is the trace.

The error kinematics can be defined by [3]

$$\dot{\widetilde{\boldsymbol{\eta}}}=\boldsymbol{G}(\widetilde{\boldsymbol{\eta}})\widetilde{\boldsymbol{V}} \tag{7}$$

where $\widetilde{\boldsymbol{V}}=\left[\Delta\boldsymbol{\omega}^{\mathrm{T}},\Delta\boldsymbol{v}^{\mathrm{T}}\right]^{\mathrm{T}}=\boldsymbol{V}-\mathrm{Ad}_{\boldsymbol{g}_e^{-1}}\boldsymbol{V}_d$ is the velocity tracking error, $\boldsymbol{V_d}$ is the desired velocity, $\mathrm{Ad}_{(\boldsymbol{g})}=\begin{bmatrix}\boldsymbol{R} & \mathbf{0}_{3\times3}\\ \boldsymbol{r}^{\times}\boldsymbol{R} & \boldsymbol{R}\end{bmatrix}\in\mathbb{R}^{6\times6}$, and $\boldsymbol{G}(\widetilde{\boldsymbol{\eta}})=\begin{bmatrix}\boldsymbol{A}(\boldsymbol{\Phi}) & \mathbf{0}_{3\times3}\\ \boldsymbol{T}(\boldsymbol{\Phi},\boldsymbol{\chi}) & \boldsymbol{A}(\boldsymbol{\Phi})\end{bmatrix}$, where

$$\boldsymbol{A}(\boldsymbol{\Phi})=\boldsymbol{I}_{3\times3}+\frac{1}{2}\boldsymbol{\Phi}^{\times}+(\frac{1}{\theta^2}-\frac{1+\cos\theta}{2\theta\sin\theta})(\boldsymbol{\Phi}^{\times})^2$$

$$\boldsymbol{T}(\boldsymbol{\Phi},\boldsymbol{\chi}) = \frac{1}{2}\big(\boldsymbol{S}(\boldsymbol{\Phi})\boldsymbol{\chi}\big)^{\times}\boldsymbol{A}(\boldsymbol{\Phi}) + \big(\frac{1}{\theta^2} - \frac{1+\cos\theta}{2\theta\sin\theta}\big)\big(\boldsymbol{\Phi}\boldsymbol{\chi}^{\mathrm{T}} + \boldsymbol{\Phi}^{\mathrm{T}}\boldsymbol{\chi}\boldsymbol{A}(\boldsymbol{\Phi})\big) - \frac{\big(1+\cos\theta\big)\big(\theta-\sin\theta\big)}{2\theta\sin^2\theta}\boldsymbol{S}(\boldsymbol{\Phi})\boldsymbol{\chi}\boldsymbol{\Phi}^{\mathrm{T}} + \Big(\frac{\big(1+\cos\theta\big)\big(\theta+\sin\theta\big)}{2\theta^3\sin^2\theta} - \frac{2}{\theta^4}\Big)\boldsymbol{\Phi}^{\mathrm{T}}\boldsymbol{\chi}\boldsymbol{\Phi}\boldsymbol{\Phi}^{\mathrm{T}}.$$

The relative acceleration of the spacecraft is given by [3]

$$\dot{\widetilde{\boldsymbol{V}}} = \dot{\boldsymbol{V}} + \mathrm{ad}_{\widetilde{\boldsymbol{V}}}\mathrm{Ad}_{\boldsymbol{g}_e^{-1}}\boldsymbol{V}_d - \mathrm{Ad}_{\boldsymbol{g}_e^{-1}}\dot{\boldsymbol{V}}_d. \tag{8}$$

Model parameter uncertainty in spacecraft systems can not be ignored [33]. Thus, $\boldsymbol{\Xi}_1 = \boldsymbol{\Xi} + \Delta\boldsymbol{\Xi}$ and $\boldsymbol{\Xi}_1^{-1} = \boldsymbol{\Xi}^{-1} + \Delta\widetilde{\boldsymbol{\Xi}}$ are used to represent the system parameters, where $\Delta\boldsymbol{\Xi}$ and $\Delta\widetilde{\boldsymbol{\Xi}}$ denote model parameter uncertainties. Then, taking Eq. (4) into Eq. (8) yields the relative 6-DOF dynamics of the spacecraft tracking system [20]

$$\dot{\widetilde{\boldsymbol{V}}} = \boldsymbol{H} + \Delta\boldsymbol{d} + \boldsymbol{\Xi}^{-1}\boldsymbol{\Gamma}_c + \boldsymbol{\Xi}^{-1}\boldsymbol{f}(\boldsymbol{\Xi}) \tag{9}$$

where $\boldsymbol{H} = \boldsymbol{\Xi}^{-1}\mathrm{ad}^*_{\boldsymbol{V}}\boldsymbol{\Xi}\boldsymbol{V} + \mathrm{ad}_{\widetilde{\boldsymbol{V}}}\mathrm{Ad}_{\boldsymbol{g}_e^{-1}}\boldsymbol{V}_d - \mathrm{Ad}_{\boldsymbol{g}_e^{-1}}\dot{\boldsymbol{V}}_d$, and $\Delta\boldsymbol{d}$ represents the total disturbance, expressed as $\Delta\boldsymbol{d} = \Delta\widetilde{\boldsymbol{\Xi}}\big(\mathrm{ad}^*_{\boldsymbol{V}}\boldsymbol{\Xi}_1\boldsymbol{V} + \boldsymbol{\Gamma}_c + \boldsymbol{f}(\boldsymbol{\Xi})\big) + \boldsymbol{\Xi}^{-1}\mathrm{ad}^*_{\boldsymbol{V}}\Delta\boldsymbol{\Xi}\boldsymbol{V} + \boldsymbol{\Xi}_1^{-1}\big(\boldsymbol{\Gamma}_d + \boldsymbol{f}(\boldsymbol{\Xi}_1) - \boldsymbol{f}(\boldsymbol{\Xi})\big)$.

C. Actuator Dynamics

The spacecraft is controlled by N low-thrust propulsion thrusters that are continuous within a saturation bound, whose dynamics are represented by [34]

$$\boldsymbol{u}_a = \boldsymbol{u}_m(\boldsymbol{f}) \tag{10}$$

where $\boldsymbol{f} = [f_1 \cdots f_N]^{\mathrm{T}} \in \mathbb{R}^N$ is thrusters' input, $\boldsymbol{u}_a = [u_{a1} \cdots u_{aN}]^{\mathrm{T}} \in \mathbb{R}^N$ is the actual output, and $\boldsymbol{u}_m(\cdot) \in \mathbb{R}^N$ denotes their mapping. Considering thruster saturation and output deviation, the expression of $\boldsymbol{u}_m$ can be obtained: $u_m(f_i) = \mathrm{sat}(f_i) + \bar{f}_i$, where $i = 1, 2, \cdots N$, $\bar{f}_i$ is the bias output of thruster i and satisfies $|\bar{f}_i| \leq f_0$, f_0 is a very small constant, and $\mathrm{sat}(f_i) = f_i + \Theta_i(f_i)$ is the saturation function. $\Theta_i(f_i)$ is defined as

$$\Theta_i(f_i) = \begin{cases} f_{\max} - f_i, & \text{if } f_i > f_{\max} \\ 0, & \text{if } |f_i| \leq f_{\max} \\ -f_{\max} - f_i, & \text{if } f_i < -f_{\max} \end{cases}$$

where $f_{\max}$ is thruster's maximum output. Then the actual control torque and force $\boldsymbol{\Gamma}_c$ in Eq. (9) can be obtained

$$\boldsymbol{\Gamma}_{c/actual} = \boldsymbol{D}\boldsymbol{u}_a = \boldsymbol{D}(\boldsymbol{f} + \boldsymbol{\Theta}(\boldsymbol{f}) + \bar{\boldsymbol{f}}) \tag{11}$$

where $\boldsymbol{D} \in \mathbb{R}^{6\times N}$ is the distribution matrix of the thrusters, and satisfies $\mathrm{rank}(\boldsymbol{D}\boldsymbol{D}^{\mathrm{T}}) = 6$. Due to limited manufacturing tolerances or warping of the spacecraft structure during launch, the uncertainty of distribution matrix exists. Therefore, $\boldsymbol{D}$ is modified to $\boldsymbol{D} + \Delta\boldsymbol{D}$, where $\Delta\boldsymbol{D}$ denotes the thruster misalignment matrix. Then, Eq. (11) can be changed to

$$\boldsymbol{\Gamma}_{c/actual} = \boldsymbol{D}\boldsymbol{f} + (\boldsymbol{D} + \Delta\boldsymbol{D})(\boldsymbol{\Theta}(\boldsymbol{f}) + \bar{\boldsymbol{f}}) + \Delta\boldsymbol{D}\boldsymbol{f} \tag{12}$$

To this end, the relative 6-DOF dynamics considering actuator dynamics can still be written in the form of Eq. (9), where $\boldsymbol{\Gamma}_c$ in (9) is written as $\boldsymbol{\Gamma}_c = \boldsymbol{D}\boldsymbol{f}$ and $\Delta\boldsymbol{d}$ is changed to $\Delta\boldsymbol{d} = \Delta\widetilde{\boldsymbol{\Xi}}\big(\mathrm{ad}^*_{\boldsymbol{V}}\boldsymbol{\Xi}_1\boldsymbol{V} + \boldsymbol{D}\boldsymbol{f} + \boldsymbol{f}(\boldsymbol{\Xi})\big) + \boldsymbol{\Xi}^{-1}\mathrm{ad}^*_{\boldsymbol{V}}\Delta\boldsymbol{\Xi}\boldsymbol{V} + \boldsymbol{\Xi}_1^{-1}\big((\boldsymbol{D}+\Delta\boldsymbol{D})(\boldsymbol{\Theta}(\boldsymbol{f})+\bar{\boldsymbol{f}}) + \Delta\boldsymbol{D}\boldsymbol{f} + \boldsymbol{\Gamma}_d + \boldsymbol{f}(\boldsymbol{\Xi}_1) - \boldsymbol{f}(\boldsymbol{\Xi})\big)$, and satisfies the following assumption. It is assumed that the disturbance of the spacecraft $\Delta\boldsymbol{d}$ is at least class C^1 piecewise differentiable, and its first-order derivative is bounded by $||\Delta\dot{\boldsymbol{d}}|| \leq \delta_1$, where δ_1 is an unknown positive constant.

The purpose of this paper is to design a controller $\boldsymbol{\Gamma}_c$ to guarantee that $\widetilde{\boldsymbol{\eta}}$ and $\widetilde{\boldsymbol{V}}$ converge to zero. It should be noted that the logarithm map is uniquely defined when $||\boldsymbol{\Phi}|| < \pi$, which means that the designed tracking controller is almost globally stable. Additionally we assume that the rank of $\boldsymbol{D}$ is 6 (fully actuated). A simple optimal way to distribute $\boldsymbol{\Gamma}_c$ to the thrusters is $\boldsymbol{f} = \boldsymbol{D}^{\dagger}\boldsymbol{\Gamma}_c$, where $\boldsymbol{D}^{\dagger} = \boldsymbol{D}^{\mathrm{T}}(\boldsymbol{D}\boldsymbol{D}^{\mathrm{T}})^{-1}$ is the pseudo-inverse matrix of $\boldsymbol{D}$ [35].

III. Adaptive Event-Triggered Controller Design and Stability Analysis

In this section, a finite-time nonlinear ESO is proposed to estimate the total disturbance, because finite-time stability permits to estimate the disturbance quickly and using nonlinear ESO yields better estimation performance than linear ESO [21]. Then, with the estimation information, an adaptive SMC is designed based on event-triggered mechanism to ensure that the spacecraft trajectory converges to a neighborhood of the desired one. Applying event-triggered control can reduce the spacecraft communication burden significantly.

A. Lemmas

In order to facilitate the stability analysis of the proposed controller, the following useful lemmas are presented.

Lemma 1. *([16]) Suppose that there exists a continuous positive Lyapunov function $V(\boldsymbol{x},t) : \mathbb{R}^n \to \mathbb{R}$ such that*

$$\dot{V}(\boldsymbol{x},t) \leq -\rho_1 V(\boldsymbol{x},t) - \rho_2 V^{\rho}(\boldsymbol{x},t), \forall t > t_0, \boldsymbol{x} \in \Omega\backslash\{\boldsymbol{0}\}$$

where $\rho_1 > 0, \rho_2 > 0$, $0 < \rho < 1$, and $\Omega \in \mathbb{R}^n$ is a neighborhood of the origin. Then, the origin is a finite-time stable point of the system, and $\boldsymbol{x}$ can converge to the equilibrium with the settling time t_f satisfying

$$t_f \leq \frac{1}{\rho_1(1-\rho)} \ln \frac{\rho_1 V^{1-\rho}(\boldsymbol{x}_0) + \rho_2}{\rho_2}$$

Lemma 2. *The matrix $\boldsymbol{G}(\widetilde{\boldsymbol{\eta}})$ is positive definite (the proof can be found in [20]).*

B. Finite-Time Extended State Observer Design

To estimate the disturbance, a novel finite-time ESO is proposed utilizing the sliding mode observer and ESO techniques. First, a fast terminal sliding mode (FTSM) is defined as $\boldsymbol{S} = \widetilde{\boldsymbol{V}} + \boldsymbol{\vartheta}_1\widetilde{\boldsymbol{\eta}} + \boldsymbol{\vartheta}_2\mathrm{sig}^{\alpha}(\widetilde{\boldsymbol{\eta}})$, where $\boldsymbol{\vartheta}_1, \boldsymbol{\vartheta}_2 \in \mathbb{R}^{6\times 6}$ are positive definite diagonal matrices, $\mathrm{sig}^{\alpha}(\widetilde{\boldsymbol{\eta}}) = [|\widetilde{\eta}_1|^{\alpha}\mathrm{sign}(\widetilde{\eta}_1), \cdots, |\widetilde{\eta}_6|^{\alpha}\mathrm{sign}(\widetilde{\eta}_6)]^{\mathrm{T}}$, $\mathrm{sign}(\cdot)$ is the sign function, and $\alpha \in (0.5, 1)$. Taking the time derivative of $\boldsymbol{S}$ and substituting (7) and (8) into it, we have $\dot{\boldsymbol{S}} = \boldsymbol{H}_1 + \boldsymbol{\Xi}^{-1}\boldsymbol{\Gamma}_c + \Delta\boldsymbol{d}$,

where $\boldsymbol{H}_1 = \boldsymbol{H} + \boldsymbol{\Xi}^{-1}\boldsymbol{f}(\boldsymbol{\Xi}) + \vartheta_1 \boldsymbol{G}(\widetilde{\boldsymbol{\eta}})\widetilde{\boldsymbol{V}} + \alpha\vartheta_2|\widetilde{\boldsymbol{\eta}}|^{\alpha-1}\boldsymbol{G}(\widetilde{\boldsymbol{\eta}})\widetilde{\boldsymbol{V}}$. Using the ESO theory in [17], defining a new state $\boldsymbol{Z}_1 = \boldsymbol{S}$, and regarding $\boldsymbol{Z}_2 = \Delta\boldsymbol{d}$ as an extended state, which satisfies $\dot{\boldsymbol{Z}}_2 = \Delta\dot{\boldsymbol{d}} = \boldsymbol{\varpi}(t)$, yield

$$\begin{cases} \dot{\boldsymbol{Z}}_1 = \boldsymbol{H}_1 + \boldsymbol{\Xi}^{-1}\boldsymbol{\Gamma}_c + \boldsymbol{Z}_2 \\ \dot{\boldsymbol{Z}}_2 = \boldsymbol{\varpi}(t) \end{cases} \tag{13}$$

Let $\hat{\boldsymbol{Z}}_1, \hat{\boldsymbol{Z}}_2$ be the estimates of $\boldsymbol{Z}_1, \boldsymbol{Z}_2$, and $\boldsymbol{e}_1 = \hat{\boldsymbol{Z}}_1 - \boldsymbol{Z}_1$, $\boldsymbol{e}_2 = \hat{\boldsymbol{Z}}_2 - \boldsymbol{Z}_2$ denote the observer errors, respectively, and then the finite time ESO can be designed as follows

$$\begin{cases} \dot{\hat{\boldsymbol{Z}}}_1 = \boldsymbol{H}_1 + \boldsymbol{\Xi}^{-1}\boldsymbol{\Gamma}_c + \hat{\boldsymbol{Z}}_2 - \boldsymbol{k}_1\beta^{\alpha_1}\mathrm{sig}^{\alpha_1}(\boldsymbol{e}_1) - \boldsymbol{k}_2\beta\boldsymbol{e}_1 \\ \dot{\hat{\boldsymbol{Z}}}_2 = -\boldsymbol{k}_3\beta^{2\alpha_1}\mathrm{sig}^{\alpha_2}(\boldsymbol{e}_1) - \boldsymbol{k}_4\beta^{\alpha_1+1}\mathrm{sig}^{\alpha_1}(\boldsymbol{e}_1) - \boldsymbol{k}_5\beta^2\boldsymbol{e}_1 \end{cases} \tag{14}$$

where $\boldsymbol{k}_i = \mathrm{diag}(k_{i1}\boldsymbol{I}_{3\times3}, k_{i2}\boldsymbol{I}_{3\times3}) \in \mathbb{R}^{6\times6} > 0, (i = 1, 2\cdots5)$ are positive definite diagonal matrices, $\beta > 0$, $\alpha_1 \in (0.5, 1)$, and $\alpha_1 = (1+\alpha_2)/2$. Then, the error dynamics can be obtained as

$$\begin{cases} \dot{\boldsymbol{e}}_1 = -\boldsymbol{k}_1\beta^{\alpha_1}\mathrm{sig}^{\alpha_1}(\boldsymbol{e}_1) - \boldsymbol{k}_2\beta\boldsymbol{e}_1 + \boldsymbol{e}_2 \\ \dot{\boldsymbol{e}}_2 = -\boldsymbol{k}_3\beta^{2\alpha_1}\mathrm{sig}^{\alpha_2}(\boldsymbol{e}_1) - \boldsymbol{k}_4\beta^{\alpha_1+1}\mathrm{sig}^{\alpha_1}(\boldsymbol{e}_1) - \boldsymbol{k}_5\beta^2\boldsymbol{e}_1 - \boldsymbol{\varpi}(t) \end{cases} \tag{15}$$

Theorem 1. *By selecting the ESO parameters such that the constraints* $\alpha_1 k_{3j}k_{5j} > k_{2j}^2 k_{3j} + \alpha_1(1+\alpha_1)^2 k_{1j}^2 k_{2j}^2$ *and* $4k_{5j}(k_{2j}k_{3j} + k_{1j}k_{4j}) > k_{2j}k_{4j}^2$ *are satisfied, where* $j = 1, 2$. *Then the observer errors will converge to*

$$\Delta_1 = \left\{ \bar{\boldsymbol{\varepsilon}} \in \mathbb{R}^3 | \, \|\bar{\boldsymbol{\varepsilon}}\| \le \left(\frac{\delta_1 \|\hbar\| \sqrt{\lambda_{\max}(\boldsymbol{P})}}{\beta\lambda_{\min}(\boldsymbol{Q}_1)\sqrt{\lambda_{\min}(\boldsymbol{P})}} \right)^{\frac{\alpha_1}{\alpha_2}} \right\} \tag{16}$$

in finite time.

Proof. Consider the following candidate Lyapunov function

$$V_1 = \frac{k_{3j}\beta^{2\alpha_1}}{\alpha_1}|e_{1i}|^{2\alpha_1} + k_{5j}\beta^2 e_{1i}^2 + \frac{e_{2i}^2}{2} + \frac{1}{2}(k_{1j}\beta^{\alpha_1}\mathrm{sig}^{\alpha_1}(e_{1i}) + k_{2j}\beta e_{1i} - e_{2i})^2 \tag{17}$$

where $i = 1, 2, \cdots 6$. By defining $\bar{\boldsymbol{\varepsilon}} = [\beta^{\alpha_1}\mathrm{sig}^{\alpha_1}(e_{1i}), \beta e_{1i}, e_{2i}]^{\mathrm{T}}$, (17) can be written as $V_1 = \bar{\boldsymbol{\varepsilon}}^{\mathrm{T}}\boldsymbol{P}\bar{\boldsymbol{\varepsilon}}$, where

$$\boldsymbol{P} = \frac{1}{2}\begin{bmatrix} 2k_{3j}/\alpha_1 + k_{1j}^2 & k_{1j}k_{2j} & -k_{1j} \\ k_{1j}k_{2j} & 2k_{5j} + k_{2j}^2 & -k_{2j} \\ -k_{1j} & -k_{2j} & 2 \end{bmatrix} > 0$$

It is obvious that V_1 is positive definite and radially unbounded, with the range $\lambda_{\min}(\boldsymbol{P})\|\bar{\boldsymbol{\varepsilon}}\|^2 \le V_1 \le \lambda_{\max}(\boldsymbol{P})\|\bar{\boldsymbol{\varepsilon}}\|^2$, where $\lambda_{\max}(\cdot)$ and $\lambda_{\min}(\cdot)$ represent the maximum and minimum eigenvalues of a matrix, respectively. Taking the

time derivative of V_1 and substituting (15) into the equation, yield

$$\begin{aligned}\dot{V}_1 =& -|e_{1i}|^{\alpha_1-1}\beta^{\alpha_1}\left[\begin{array}{l}(k_{1j}k_{3j}+\alpha_1 k_{1j}^3)\beta^{2\alpha_1}|e_{1i}|^{2\alpha_1}+(k_{1j}k_{5j}+(2+\alpha_1)k_{1j}k_{2j}^2)\beta^2|e_{1i}|^2\\ +\alpha_1 k_{1j}e_{2i}^2-2(\alpha_1+1)\beta k_{1j}k_{2j}e_{1i}e_{2i}-2\alpha_1\beta^{\alpha_1}k_{1j}^2\mathrm{sig}^{\alpha_1}(e_{1i})e_{2i}\end{array}\right]\\ &-\beta\left[\begin{array}{l}k_{2j}e_{2i}^2+(k_{2j}k_{5j}+k_{2j}^3)\beta^2e_{1i}^2+(k_{2j}k_{3j}+2\alpha_1k_{2j}k_{1j}^2+k_{1j}^2k_{2j}-k_{1j}k_{4j})\beta^{2\alpha_1}|e_{1i}|^{2\alpha_1}\\ -2\beta k_{2j}^2e_{1i}e_{2i}-k_{2j}k_{4j}\beta^{\alpha_1+1}|e_{1i}|^{\alpha_1+1}+2k_{4j}\beta^{\alpha_1}\mathrm{sig}^{\alpha_1}(e_{1i})e_{2i}\end{array}\right]\\ &+k_{1j}\beta^{\alpha_1}\mathrm{sig}^{\alpha_1}(e_{1i})\varpi_i(t)-2e_{2i}\varpi_i(t)+\beta k_{2j}e_{1i}\varpi_i(t)\\ &=-|e_{1i}|^{\alpha_1-1}\beta^{\alpha_1}\bar{\boldsymbol{\varepsilon}}^{\mathrm{T}}\boldsymbol{Q}_1\bar{\boldsymbol{\varepsilon}}-\beta\bar{\boldsymbol{\varepsilon}}^{\mathrm{T}}\boldsymbol{Q}_2\bar{\boldsymbol{\varepsilon}}+\varpi_i(t)\hbar\bar{\boldsymbol{\varepsilon}}\end{aligned}\tag{18}$$

where $\hbar=[k_{1j},k_{2j},-2]$, $\boldsymbol{Q}_1=k_{1j}\left[\begin{array}{ccc}k_{3j}+\alpha_1k_{1j}^2 & 0 & -\alpha_1k_{1j}\\ 0 & k_{5j}+(2+\alpha_1)k_{2j}^2 & -(1+\alpha_1)k_{2j}\\ -\alpha_1k_{1j} & -(1+\alpha_1)k_{2j} & \alpha_1\end{array}\right]$,

and $\boldsymbol{Q}_2=\left[\begin{array}{ccc}k_{2j}k_{3j}+(2\alpha_1+1)k_{2j}k_{1j}^2+k_{1j}k_{4j} & -k_{2j}k_{4j}/2 & k_{4j}\\ -k_{2j}k_{4j}/2 & k_{2j}k_{5j}+k_{2j}^3 & -k_{2j}^2\\ k_{4j} & -k_{2j}^2 & k_{2j}\end{array}\right]$.

When the constraints in Theorem 1 are satisfied, $\boldsymbol{Q}_1>0$, $\boldsymbol{Q}_2>0$. Using the inequality $\beta^{\alpha_1-1}|e_{1i}|^{\alpha_1-1}\geq||\bar{\boldsymbol{\varepsilon}}||^{\frac{\alpha_1-1}{\alpha_1}}$ and $V_1/\lambda_{\max}(\boldsymbol{P})\leq||\bar{\boldsymbol{\varepsilon}}||$, we have

$$\begin{aligned}\dot{V}_1&\leq-\beta\lambda_{\min}(\boldsymbol{Q}_1)||\bar{\boldsymbol{\varepsilon}}||^{\frac{3\alpha_1-1}{\alpha_1}}-\beta\lambda_{\min}(\boldsymbol{Q}_2)||\bar{\boldsymbol{\varepsilon}}||^2+\delta_1||\hbar||||\bar{\boldsymbol{\varepsilon}}||\\ &\leq-\Big(\frac{\beta\lambda_{\min}(\boldsymbol{Q}_1)}{\sqrt{\lambda_{\max}(\boldsymbol{P})}}||\bar{\boldsymbol{\varepsilon}}||^{\frac{2\alpha_1-1}{\alpha_1}}-\frac{\delta_1||\hbar||}{\sqrt{\lambda_{\min}(\boldsymbol{P})}}\Big)V_1^{1/2}-\frac{\beta\lambda_{\min}(\boldsymbol{Q}_2)}{\sqrt{\lambda_{\max}(\boldsymbol{P})}}V_1\end{aligned}\tag{19}$$

From Lemma 1, we conclude that the observer errors can converge to Δ_1 in finite time. It should be noted that Δ_1 can be as small as desirable by choosing suitable $\boldsymbol{k}_i$ and β such that $\frac{\delta_1\|\hbar\|\sqrt{\lambda_{\max}(\boldsymbol{P})}}{\beta\lambda_{\min}(\boldsymbol{Q}_1)\sqrt{\lambda_{\min}(\boldsymbol{P})}}\ll1$ and $\alpha_1/\alpha_2>1$ with $\alpha_1\in(0.5,1)$ to guarantee the high accuracy of ESO. Since $\boldsymbol{P}$ and $\boldsymbol{Q}_1$ are two matrices related to $\boldsymbol{k}_{ij}$, a method to design the parameters in simulation is that once β is fixed, smaller $\boldsymbol{k}_{1j}$, $\boldsymbol{k}_{2j}$, and larger $\boldsymbol{k}_{3j}$, $\boldsymbol{k}_{4j}$, $\boldsymbol{k}_{5j}$ are required, while the constraints on $\boldsymbol{k}_{ij}$ should be satisfied. □

Remark 1. *The observer in [19] provides a fast local convergence only when the observer errors are near the origin. However in this paper the linear terms $\boldsymbol{k}_2\beta\boldsymbol{e}_1$, $\boldsymbol{k}_5\beta^2\boldsymbol{e}_1$ in (15) are shown to improve the dynamical performance. When $\boldsymbol{e}_1,\boldsymbol{e}_2$ are far from the origin, the linear terms dominate over the nonlinear ones such that the observer error can converge exponentially fast. Moreover, compared with the observer in [20], the nonlinear term $\boldsymbol{k}_4\beta^{\alpha_1+1}\mathrm{sig}^{\alpha_1}(\boldsymbol{e}_1)$ is added to improve the observer performance when its errors are near the origin. Furthermore, the parameters in (15) have been changed from $\boldsymbol{k}_i$ to $\boldsymbol{k}_i\beta^{\alpha_j}$, which permits a simple switch between linear ESO and nonlinear ESO. When $k_{1j}=k_{3j}=k_{4j}=0$, $k_{2j}=3$, and $k_{5j}=2$, the observer will reduce to a linear ESO of [17], where β is the observer bandwidth. This means that the type of the observer can be selected according to the control accuracy requirement of the investigated problem, with the flexibility to trade off higher accuracy with design complexity of the observer.*

C. ESO Based Adaptive Event-Triggered Sliding Mode Controller Synthesis

Let $\{t_k\}_{=0}^{\infty}, t_0 = 0$ be the triggering time sequences generated by the event-triggering strategy. The control signal $\boldsymbol{\Gamma}_c$ is updated at t_k and will be held constant through a zero-order holder (ZOH) when $t \in [t_k, t_{k+1})$, namely

$$\boldsymbol{\Gamma}_c(t) = \boldsymbol{\Gamma}_{cout}(t_k), t \in [t_k, t_{k+1}) \tag{20}$$

where $\boldsymbol{\Gamma}_{cout}$ is the designed controller. The proposed triggering strategy is based on the measurement error of the control signal $\boldsymbol{e}_c = \boldsymbol{\Gamma}_c(t) - \boldsymbol{\Gamma}_{cout}(t)$, and the triggering time is determined by

$$t_{k+1} = \inf\Big\{t > t_k \Big| \big\|\bar{\boldsymbol{e}}_{c1}\big\| \geq a_1\big\|\bar{\boldsymbol{S}}_1\big\| + \gamma_1, \text{or } \big\|\bar{\boldsymbol{e}}_{c2}\big\| \geq a_2\big\|\bar{\boldsymbol{S}}_2\big\| + \gamma_2\Big\} \tag{21}$$

where $a_1 > 0$, $a_2 > 0$, $\gamma_1 > 0$, $\gamma_2 > 0$, $\bar{\boldsymbol{e}}_{c1} = [e_{c1}, e_{c2}, e_{c3}]^{\mathrm{T}}$, $\bar{\boldsymbol{e}}_{c2} = [e_{c4}, e_{c5}, e_{c6}]^{\mathrm{T}}$, $\bar{\boldsymbol{S}}_1 = [S_1, S_2, S_3]^{\mathrm{T}}$, and $\bar{\boldsymbol{S}}_2 = [S_4, S_5, S_6]^{\mathrm{T}}$. Moreover, since the control signal has to be distributed to the thrusters simultaneously, the control force and torque signals have to be triggered at the same time. Based on the above introduction, the proposed adaptive event-triggered controller and its stability analysis will be stated in the following theorem.

Theorem 2. *The adaptive event-triggered FTSM controller is designed as follows*

$$\boldsymbol{\Gamma}_{cout}(t) = -\boldsymbol{\Xi}\big(\boldsymbol{H}_1 + \hat{\boldsymbol{Z}}_2\big) - \boldsymbol{K}_1 \mathrm{sig}^{\alpha}(\boldsymbol{S}) - \big(\boldsymbol{K}_2 + \boldsymbol{K}_3(\|\boldsymbol{S}\|)\big)\boldsymbol{S} \tag{22}$$

where $\hat{\boldsymbol{Z}}_2$ is the ESO output, $\boldsymbol{K}_1 = \mathrm{diag}(K_{11}\boldsymbol{I}_{3\times3}, K_{12}\boldsymbol{I}_{3\times3}) \in \mathbb{R}^{6\times6} > 0$, $\boldsymbol{K}_2 = \mathrm{diag}(K_{21}\boldsymbol{I}_{3\times3}, K_{22}\boldsymbol{I}_{3\times3}) \in \mathbb{R}^{6\times6}$ with $K_{21} > a_1$ and $K_{22} > a_2$, $\boldsymbol{K}_3(\|\boldsymbol{S}\|) = \mathrm{diag}(K_{31}\boldsymbol{I}_{3\times3}, K_{32}\boldsymbol{I}_{3\times3}) \in \mathbb{R}^{6\times6}$, and K_{31}, K_{32} are positive adaptive gain parameters designed as follows:

$$K_{31} = \frac{\hat{\varphi}_1 + \ell_1 \int_{t_k}^{t} \hat{\varphi}_1(s)ds}{\big\|\bar{\boldsymbol{S}}_1\big\| + \epsilon_1 \exp\left(-\sigma_1 t\right)};\ K_{32} = \frac{\hat{\varphi}_2 + \ell_2 \int_{t_k}^{t} \hat{\varphi}_2(s)ds}{\big\|\bar{\boldsymbol{S}}_2\big\| + \epsilon_2 \exp\left(-\sigma_2 t\right)} \tag{23}$$

where $t \in [t_k, t_{k+1})$. φ_1, φ_2 are the upper bounds of $\big\|\bar{\boldsymbol{e}}_{21}\big\| + \gamma_1$ and $\big\|\bar{\boldsymbol{e}}_{22}\big\| + \gamma_2$, where $\bar{\boldsymbol{e}}_{21} = \boldsymbol{J} \cdot [e_{21}, e_{22}, e_{23}]^{\mathrm{T}}$, and $\bar{\boldsymbol{e}}_{22} = m \cdot [e_{24}, e_{25}, e_{26}]^{\mathrm{T}}$. $\hat{\varphi}_1, \hat{\varphi}_2$ are the estimated values of φ_1, φ_2, which are updated by:

$$\dot{\hat{\varphi}}_1 = -\ell_1\hat{\varphi}_1 + \frac{\big\|\bar{\boldsymbol{S}}_1\big\|^2}{\big\|\bar{\boldsymbol{S}}_1\big\| + \epsilon_1 \exp\left(-\sigma_1 t\right)};\ \dot{\hat{\varphi}}_2 = -\ell_2\hat{\varphi}_2 + \frac{\big\|\bar{\boldsymbol{S}}_2\big\|^2}{\big\|\bar{\boldsymbol{S}}_2\big\| + \epsilon_2 \exp\left(-\sigma_2 t\right)} \tag{24}$$

where $\epsilon_1 > 0$, $\epsilon_2 > 0$, $\ell_1 > 0$, $\ell_2 > 0$, $\sigma_1 > 0$, and $\sigma_2 > 0$. Then, the spacecraft tracking maneuver can be achieved asymptotically. Moreover, the Zeno behaviour is avoided.

Proof. The following Lyapunov function is considered

$$V_2 = \frac{1}{2}\boldsymbol{S}^{\mathrm{T}}\boldsymbol{\Xi}\boldsymbol{S} + \frac{1}{2}\widetilde{\varphi}_1^2 + \frac{1}{2}\widetilde{\varphi}_2^2 \tag{25}$$

where $\widetilde{\varphi}_1 = \varphi_1 - \hat{\varphi}_1 - \ell_1 \int_{t_k}^{t} \hat{\varphi}_1(s)ds$ and $\widetilde{\varphi}_2 = \varphi_2 - \hat{\varphi}_2 - \ell_2 \int_{t_k}^{t} \hat{\varphi}_2(s)ds$. Taking the derivative of V_2 with respect

to time $t \in [t_k, t_{k+1})$ and using controller (22) yield

$$\begin{aligned}\dot{V}_2 &= \boldsymbol{S}^{\mathrm{T}}\boldsymbol{\Xi}\dot{\boldsymbol{S}} + \widetilde{\varphi}_1\dot{\widetilde{\varphi}}_1 + \widetilde{\varphi}_2\dot{\widetilde{\varphi}}_2 \\ &= \boldsymbol{S}^{\mathrm{T}}\boldsymbol{\Xi}(\boldsymbol{H}_1 + \boldsymbol{\Xi}^{-1}(\boldsymbol{\Gamma}_{cout}(t) + \boldsymbol{e}_c) + \Delta\boldsymbol{d}) + \widetilde{\varphi}_1\dot{\widetilde{\varphi}}_1 + \widetilde{\varphi}_2\dot{\widetilde{\varphi}}_2 \\ &= -\boldsymbol{S}^{\mathrm{T}}\boldsymbol{\Xi}(\hat{\boldsymbol{Z}}_2 - \Delta\boldsymbol{d}) - \boldsymbol{S}^{\mathrm{T}}\boldsymbol{K}_1\mathrm{sig}^{\alpha}(\boldsymbol{S}) - \boldsymbol{S}^{\mathrm{T}}\big(\boldsymbol{K}_2 + \boldsymbol{K}_3(\|\boldsymbol{S}\|)\big)\boldsymbol{S} + \boldsymbol{S}^{\mathrm{T}}\boldsymbol{e}_c + \widetilde{\varphi}_1\dot{\widetilde{\varphi}}_1 + \widetilde{\varphi}_2\dot{\widetilde{\varphi}}_2\end{aligned} \tag{26}$$

Substituting the triggering strategy in (21) and the control gains in (23) into (26) leads to

$$\begin{aligned}\dot{V}_2 \leq\ & -(K_{21}-a_1)\big\|\bar{\boldsymbol{S}}_1\big\|^2 - (K_{22}-a_2)\big\|\bar{\boldsymbol{S}}_2\big\|^2 + \big(\|\bar{e}_{21}\| + \gamma_1\big)\big\|\bar{\boldsymbol{S}}_1\big\| + \big(\|\bar{e}_{22}\| + \gamma_2\big)\big\|\bar{\boldsymbol{S}}_2\big\| \\ & - \frac{\hat{\varphi}_1 + \ell_1\int_{t_k}^{t}\hat{\varphi}_1(s)ds}{\big\|\bar{\boldsymbol{S}}_1\big\| + \epsilon_1\exp(-\sigma_1 t)}\big\|\bar{\boldsymbol{S}}_1\big\|^2 - \frac{\hat{\varphi}_2 + \ell_2\int_{t_k}^{t}\hat{\varphi}_2(s)ds}{\big\|\bar{\boldsymbol{S}}_2\big\| + \epsilon_2\exp(-\sigma_2 t)}\big\|\bar{\boldsymbol{S}}_2\big\|^2 - \boldsymbol{S}^{\mathrm{T}}\boldsymbol{K}_1\mathrm{sig}^{\alpha}(\boldsymbol{S}) + \widetilde{\varphi}_1\dot{\widetilde{\varphi}}_1 + \widetilde{\varphi}_2\dot{\widetilde{\varphi}}_2 \\ \leq\ & -(K_{21}-a_1)\big\|\bar{\boldsymbol{S}}_1\big\|^2 - (K_{22}-a_2)\big\|\bar{\boldsymbol{S}}_2\big\|^2 - \boldsymbol{S}^{\mathrm{T}}\boldsymbol{K}_1\mathrm{sig}^{\alpha}(\boldsymbol{S}) + \widetilde{\varphi}_1\dot{\widetilde{\varphi}}_1 + \widetilde{\varphi}_2\dot{\widetilde{\varphi}}_2 \\ & + \frac{(\varphi_1 - \hat{\varphi}_1 - \ell_1\int_{t_k}^{t}\hat{\varphi}_1(s)ds)\big\|\bar{\boldsymbol{S}}_1\big\|^2 + \epsilon_1\varphi_1\big\|\bar{\boldsymbol{S}}_1\big\|\exp(-\sigma_1 t)}{\big\|\bar{\boldsymbol{S}}_1\big\| + \epsilon_1\exp(-\sigma_1 t)} \\ & + \frac{(\varphi_2 - \hat{\varphi}_2 - \ell_2\int_{t_k}^{t}\hat{\varphi}_2(s)ds)\big\|\bar{\boldsymbol{S}}_2\big\|^2 + \epsilon_2\varphi_2\big\|\bar{\boldsymbol{S}}_2\big\|\exp(-\sigma_2 t)}{\big\|\bar{\boldsymbol{S}}_2\big\| + \epsilon_2\exp(-\sigma_2 t)}\end{aligned} \tag{27}$$

Denoting $c_1 = K_{21} - a_1 > 0$, and $c_2 = K_{22} - a_2 > 0$, and substituting the adaptive law (24) into (27), we can obtain

$$\begin{aligned}\dot{V}_2 \leq\ & -c\big\|\boldsymbol{S}\big\|^2 - \frac{(\varphi_1 - \hat{\varphi}_1 - \ell_1\int_{t_k}^{t}\hat{\varphi}_1(s)ds)\big\|\bar{\boldsymbol{S}}_1\big\|^2}{\big\|\bar{\boldsymbol{S}}_1\big\| + \epsilon_1\exp(-\sigma_1 t)} - \frac{(\varphi_2 - \hat{\varphi}_2 - \ell_2\int_{t_k}^{t}\hat{\varphi}_2(s)ds)\big\|\bar{\boldsymbol{S}}_2\big\|^2}{\big\|\bar{\boldsymbol{S}}_2\big\| + \epsilon_2\exp(-\sigma_2 t)} \\ & + \frac{(\varphi_1 - \hat{\varphi}_1 - \ell_1\int_{t_k}^{t}\hat{\varphi}_1(s)ds)\big\|\bar{\boldsymbol{S}}_1\big\|^2 + \epsilon_1\varphi_1\big\|\bar{\boldsymbol{S}}_1\big\|\exp(-\sigma_1 t)}{\big\|\bar{\boldsymbol{S}}_1\big\| + \epsilon_1\exp(-\sigma_1 t)} \\ & + \frac{(\varphi_2 - \hat{\varphi}_2 - \ell_2\int_{t_k}^{t}\hat{\varphi}_2(s)ds)\big\|\bar{\boldsymbol{S}}_2\big\|^2 + \epsilon_2\varphi_2\big\|\bar{\boldsymbol{S}}_2\big\|\exp(-\sigma_2 t)}{\big\|\bar{\boldsymbol{S}}_2\big\| + \epsilon_2\exp(-\sigma_2 t)} \\ \leq\ & -c\big\|\boldsymbol{S}\big\|^2 + \frac{\epsilon_1\varphi_1\big\|\bar{\boldsymbol{S}}_1\big\|\exp(-\sigma_1 t)}{\big\|\bar{\boldsymbol{S}}_1\big\| + \epsilon_1\exp(-\sigma_1 t)} + \frac{\epsilon_2\varphi_2\big\|\bar{\boldsymbol{S}}_2\big\|\exp(-\sigma_2 t)}{\big\|\bar{\boldsymbol{S}}_2\big\| + \epsilon_2\exp(-\sigma_2 t)}\end{aligned} \tag{28}$$

where $c = \min\{c_1, c_2\}$. Since $\epsilon_1\exp(-\sigma_1 t) > 0$ and $\epsilon_2\exp(-\sigma_2 t) > 0$, thus we have

$$\frac{\epsilon_1\varphi_1\big\|\bar{\boldsymbol{S}}_1\big\|\exp(-\sigma_1 t)}{\big\|\bar{\boldsymbol{S}}_1\big\| + \epsilon_1\exp(-\sigma_1 t)} < \epsilon_1\varphi_1\exp(-\sigma_1 t), \text{and } \frac{\epsilon_2\varphi_2\big\|\bar{\boldsymbol{S}}_2\big\|\exp(-\sigma_2 t)}{\big\|\bar{\boldsymbol{S}}_2\big\| + \epsilon_2\exp(-\sigma_2 t)} < \epsilon_2\varphi_2\exp(-\sigma_2 t)$$

Then (28) can be changed to

$$\dot{V}_2 \quad \leq -c\big\|\boldsymbol{S}\big\|^2 + \epsilon_1\varphi_1\exp(-\sigma_1 t) + \epsilon_2\varphi_2\exp(-\sigma_2 t) \tag{29}$$

Consequently, $\boldsymbol{S}$ will converge to Δ_2 asymptotically:

$$\Delta_2 = \Big\{\boldsymbol{S} \in \mathbb{R}^6 \big|\ \|\boldsymbol{S}\| \leq \sqrt{\frac{\epsilon_1\varphi_1\exp(-\sigma_1 t) + \epsilon_2\varphi_2\exp(-\sigma_2 t)}{c}}\Big\} \tag{30}$$

Due to $\sigma_1 > 0$ and $\sigma_2 > 0$, Δ_2 will decrease with time increasing. Thus, we can conclude that $\lim_{t\to+\infty}\Delta_2 = 0$

and $\lim_{t\to+\infty}\boldsymbol{S}=\mathbf{0}$, which means that when $t\to+\infty$ the following equation holds

$$\boldsymbol{S}=\widetilde{\boldsymbol{V}}+\boldsymbol{\vartheta}_1\widetilde{\boldsymbol{\eta}}+\boldsymbol{\vartheta}_2\mathrm{sig}^{\alpha}(\widetilde{\boldsymbol{\eta}})=\mathbf{0} \tag{31}$$

Then another Lyapunov function $V_3=\frac{1}{2}\widetilde{\boldsymbol{\eta}}^{\mathrm{T}}\widetilde{\boldsymbol{\eta}}$ is considered to prove the convergence of $\widetilde{\boldsymbol{V}}$ and $\widetilde{\boldsymbol{\eta}}$. Taking the time derivative of V_3 and substituting (31) into it, yield

$$\dot{V}_3=\widetilde{\boldsymbol{\eta}}^{\mathrm{T}}\dot{\widetilde{\boldsymbol{\eta}}}=\widetilde{\boldsymbol{\eta}}^{\mathrm{T}}\boldsymbol{G}(\widetilde{\boldsymbol{\eta}})\big(-\boldsymbol{\vartheta}_1\widetilde{\boldsymbol{\eta}}-\boldsymbol{\vartheta}_2\mathrm{sig}^{\alpha}(\widetilde{\boldsymbol{\eta}})\big)\leq-\overline{\vartheta}_1V_3-\overline{\vartheta}_2V_3^{\frac{1+\alpha}{2}} \tag{32}$$

where $\overline{\vartheta}_1=2\lambda_{\min}\big(\boldsymbol{G}(\widetilde{\boldsymbol{\eta}})\boldsymbol{\vartheta}_1\big)$, and $\overline{\vartheta}_2=2^{(1+\alpha)/2}\lambda_{\min}\big(\boldsymbol{G}(\widetilde{\boldsymbol{\eta}})\boldsymbol{\vartheta}_2\big)$. Using Lemma 2, $\overline{\vartheta}_1>0$ and $\overline{\vartheta}_2>0$. Since $0.5<\alpha<1$, thus the constraints in Lemma 1 for a system to be finite-time stable are all satisfied, from which we can conclude that $\lim_{t\to+\infty}\widetilde{\boldsymbol{V}}=\lim_{t\to+\infty}\widetilde{\boldsymbol{\eta}}=\mathbf{0}$. The triggering sequence t_k is admissible if the inter-event time $t_{k+1}-t_k$ is lower bounded by a positive value. If the minimum inter-event time is zero, the triggering strategy will be motivated infinitely within a finite time interval, which leads to the so-called Zeno behavior [27]. This is critical for spacecraft control since actuator cannot be executed continuously in practice [24]. Thus, the triggering strategy without Zeno phenomenon should be guaranteed. Now we will show that for $\forall k$, there exists $t^*>0$ such that $t_{k+1}-t_k\geq t^*$. Recalling $\boldsymbol{e}_c=\boldsymbol{\Gamma}_c(t)-\boldsymbol{\Gamma}_{cout}(t)$ and $\boldsymbol{\Gamma}_c(t)$ is a constant for a certain time interval, we have

$$\frac{d}{dt}\|\boldsymbol{e}_c\|=\frac{d}{dt}\sqrt{\boldsymbol{e}_c^{\mathrm{T}}\boldsymbol{e}_c}=\frac{\boldsymbol{e}_c^{\mathrm{T}}}{||\boldsymbol{e}_c||}\dot{\boldsymbol{e}}_c\leq\|\dot{\boldsymbol{e}}_c\|=\|\dot{\boldsymbol{\Gamma}}_{cout}(t)\| \tag{33}$$

The components of $\boldsymbol{\Gamma}_{cout}$ namely, $\boldsymbol{H}_1$, $\hat{\boldsymbol{Z}}_2$ and $\boldsymbol{S}$ are all differentiable and bounded. Thus there exists a positive constant $\bar{c}$, such that $\|\dot{\boldsymbol{\Gamma}}_{cout}(t)\|\leq\bar{c}$ when $t<+\infty$. Integrating both sides of (33), yields

$$\|\boldsymbol{e}_c\|=\int_{t_k}^{t}\|\dot{\boldsymbol{\Gamma}}_{cout}(s)\|ds\leq(t-t_k)\bar{c} \tag{34}$$

which means that $\lim_{t\to t_{k+1}}(t-t_k)=t^*\geq\frac{\|\boldsymbol{e}_c\|}{\bar{c}}$. Since $\|\boldsymbol{e}_c\|>0$ and $\bar{c}>0$, thus $t^*>0$ and the Zeno behavior can be excluded successfully. Thereby, the proof of Theorem 2 has been completed. □

Remark 2. *The error $\boldsymbol{e}_c$ plays an important role in the implementation of the event-triggered controller, because t_k is generated by monitoring the value of $\boldsymbol{e}_c$ until it reaches the state-dependent relative threshold. The last transmitted control signal $\boldsymbol{\Gamma}_c$ will be held through a ZOH and distributed to each thruster before the next transmission is received. Though both the controller (22) and the controller in [20] contain the term $\boldsymbol{K}_2\boldsymbol{S}$, their functions are different. In [20], $\boldsymbol{K}_2\boldsymbol{S}$ is used to improve the convergence speed of the controller. In the event-triggered controller, $\boldsymbol{K}_2\boldsymbol{S}$ is used in combination with the adaptive laws for $\boldsymbol{K}_{3j}$ to guarantee the stability of the closed-loop system integrated with the event-triggering strategy (21). Here, a relative threshold strategy (21) motivated by [26] is applied. The triggering rule is designed based on the measurement error on the control signal, and the existence of γ_j permits that the ISS assumption on the measurement error is not required. In addition, γ_j is crucial to guarantee that t^* is still lower bounded even if $\boldsymbol{S}$ converges to zero such that Zeno behavior can be avoided. The triggering time can be adjusted by suitably designing a_j and γ_j. Larger the values of a_j and γ_j, longer the inter-update times will be generated, resulting in less communication burden, but the control performance will be worse. Therefore, a*

trade-off should be made between the communication burden and the control performance.

IV. Simulation Results

A numerical example is presented to validate the proposed controller with an application to a micro-spacecraft with low-thrust propulsion. The spacecraft needs to track the trajectory of a virtual leader. The virtual leader is assumed to operate in a circle orbit with altitude 400 km and inclination 45°, and its body fixed frame is always perfectly aligned with $\mathscr{F}_o$. The model parameters of the spacecraft are assumed to be: $\boldsymbol{J} = [\ 20\ 1\ 0.5; 1\ 21\ 0.8; 0.5\ 0.8\ 20.5\ ]\mathrm{kg}\cdot\mathrm{m}^2$, $m = 100\mathrm{kg}$, $\Delta\boldsymbol{J} = 0.1\boldsymbol{J}$, and $\Delta m = 5\mathrm{kg}$. 12 thrusters are placed paralleling to the body axes of the spacecraft, and the actuator configuration matrix $\boldsymbol{D}$ in Eq.(35) is the same as [36], where $d_x = d_y = d_z = 0.5\mathrm{m}$ are the moment arms of the thrusters with respect to the mass center of the spacecraft, $\Delta D_{ij} = 0.01\mathrm{rand}(\cdot)$, where $\mathrm{rand}(\cdot)$ generates a random value from the normal distribution with mean 0 and standard deviation 1, $f_{\max} = 0.5\mathrm{N}$, and $\bar{f}_i = 0.005 f_i$.

$$\boldsymbol{D} = \begin{bmatrix} 0 & d_z & -d_y & 0 & d_z & -d_y & 0 & -d_z & d_y & 0 & -d_z & d_y \\ d_z & 0 & -d_x & -d_z & 0 & d_x & d_z & 0 & -d_x & -d_z & 0 & d_x \\ -d_y & d_x & 0 & d_y & -d_x & 0 & d_y & -d_x & 0 & -d_y & d_x & 0 \\ -1 & 0 & 0 & -1 & 0 & 0 & 1 & 0 & 0 & 1 & 0 & 0 \\ 0 & 1 & 0 & 0 & -1 & 0 & 0 & 1 & 0 & 0 & -1 & 0 \\ 0 & 0 & 1 & 0 & 0 & -1 & 0 & 0 & -1 & 0 & 0 & 1 \end{bmatrix} \tag{35}$$

Since the spacecraft operates in a low Earth orbit (LEO), typical perturbative torques and forces mainly generated by atmospheric drag and solar radial pressure force are considered, which can be calculated as in [37]. In the simulations, the external disturbances that the spacecraft suffers are assumed to be

$$\boldsymbol{d}_\tau = 10^{-3}\cdot[1.2+\sin(0.12t+1),\ 1.5+\cos(0.15t+1),\ 1+\sin(0.18t+1)]\mathrm{N}\cdot\mathrm{m}$$

$$\boldsymbol{d}_f = 10^{-4}\cdot[4+5\sin(2\pi\|\boldsymbol{\omega}_d\|t),\ 4.5+5\cos(2\pi\|\boldsymbol{\omega}_d\|t),\ 3+\sin(2\pi\|\boldsymbol{\omega}_d\|t+\pi/3)]^{\mathrm{T}}\mathrm{N}$$

where $\boldsymbol{\omega}_d$ is the angular velocity of the virtual leader. Here, the constant torques and forces are induced by the atmospheric drag.

Two cases are considered: Case 1 is used to illustrate that different starting points of attitude and position errors will not affect the final configuration tracking accuracy, and the performance of the observer proposed in this paper has been improved compared with the previously published observer in [19]. Case 2 is used to show the role of γ_j in the balance of the control performance and the communication burden. For Case 1, two points of initial tracking errors are selected: Point 1 (P1), $\boldsymbol{\Phi} = [76.71, -14.02, 60.05]^{\mathrm{T}}\mathrm{deg}$, $\boldsymbol{\chi} = [3.61, -28.7, -9.82]^{\mathrm{T}}\mathrm{m}$, and $\widetilde{\boldsymbol{V}} = 0$; Point 2 (P2), $\boldsymbol{\Phi} = [63.6, -13.2, 51.0]^{\mathrm{T}}\mathrm{deg}$, $\boldsymbol{\chi} = [-3.4, -55.8, 0.1]^{\mathrm{T}}\mathrm{m}$, and $\widetilde{\boldsymbol{V}} = 0$. The event-triggering strategy parameters are: $a_1 = 0.6$, $a_2 = 0.8$, $\gamma_1 = 0.001$, and $\gamma_2 = 0.003$. And $\gamma_1 = 0.1$, $\gamma_2 = 0.2$ will be used for comparison in Case 2. To guarantee the stability of the ESO (14) and the controller (22), the control gains are designed as follows: (a) The sliding surface parameters are: $\boldsymbol{\vartheta}_1 = \mathrm{diag}(0.1\boldsymbol{I}_3, 0.02\boldsymbol{I}_3)$, $\boldsymbol{\vartheta}_2 = \mathrm{diag}(0.1\boldsymbol{I}_3, 0.05\boldsymbol{I}_3)$, and $\alpha = 2/3$; (b) The ESO parameters are: $\beta = 0.125$, $\alpha_1 = 2/3$, $\alpha_2 = 1/3$, $k_{11} = 0.8$, $k_{12} = 1.2$, $k_{21} = 0.24$, $k_{22} = 0.4$, $k_{31} = 1.3$, $k_{32} = 1$, $k_{41} = 1.3$, $k_{42} = 0.7$, $k_{51} = 4.5$, and $k_{52} = 3.2$; (c) The adaptive controller

parameters are: $\boldsymbol{K}_1 = \mathrm{diag}(6\boldsymbol{I}_3, 8\boldsymbol{I}_3)$, $\boldsymbol{K}_2 = \mathrm{diag}(3.2\boldsymbol{I}_3, 3.6\boldsymbol{I}_3)$, $\ell_1 = \ell_2 = 0.1$, $\epsilon_1 = \epsilon_2 = 1$, $\sigma_1 = \sigma_2 = 0.5$, $\hat{\varphi}_1(0) = 1$ and $\hat{\varphi}_2(0) = 1.2$. For the observers comparison, we set $\boldsymbol{k}_2 = \boldsymbol{k}_4 = \boldsymbol{k}_5 = 0$. Simulation results are presented in Figs. 1-12.

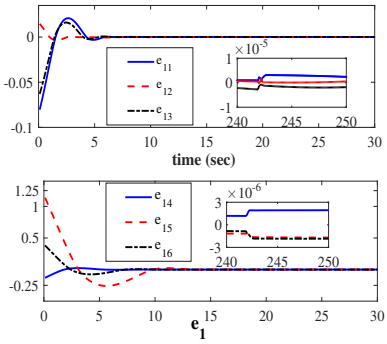

Fig. 1: Time responses of the observer error $\boldsymbol{e}_1$ (P1)

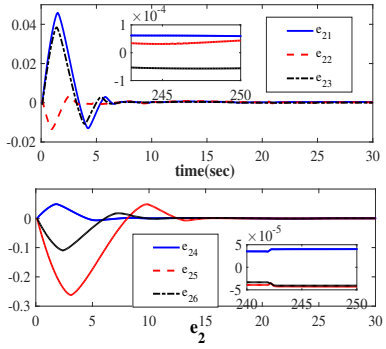

Fig. 2: Time responses of the observer error $\boldsymbol{e}_2$ (P1)

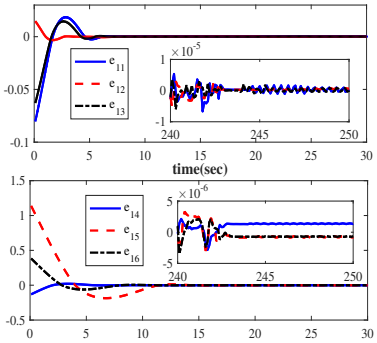

Fig. 3: Time responses of the observer error $\boldsymbol{e}_1$ using the estimator in Ref. [19] (P1)

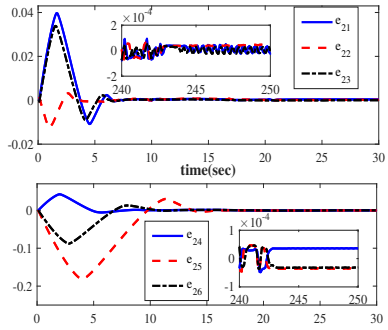

Fig. 4: Time responses of the observer error $\boldsymbol{e}_2$ using the estimator in Ref. [19] (P1)

Figs. 1 and 2 show the time responses of the observer errors of P1, where $\boldsymbol{e}_1$ is the observation error of the sliding surface $\boldsymbol{S}$, and $\boldsymbol{e}_2$ is the observation error of $\Delta\boldsymbol{d}$. From the plots of $\boldsymbol{e}_1$ and $\boldsymbol{e}_2$, we can conclude that $\boldsymbol{S}$ and $\Delta\boldsymbol{d}$ can be estimated by the ESO successfully in finite time. $\hat{\boldsymbol{Z}}_1$ tracks $\boldsymbol{S}$ in 10s, and the total disturbance $\Delta\boldsymbol{d}$ is reconstructed by $\hat{\boldsymbol{Z}}_2$ within 15s. From the steady-state behaviors of the ESO, we can find that the errors will converge to a very small region with $|\boldsymbol{e}_{1i}| < 1 \times 10^{-5}$, $|\boldsymbol{e}_{2i}| < 1 \times 10^{-4}(\mathrm{N}\cdot\mathrm{m}), i = 1, 2, 3$; $|\boldsymbol{e}_{1i}| < 3 \times 10^{-6}$, $|\boldsymbol{e}_{2i}| < 5 \times 10^{-5}(\mathrm{N}), i = 4, 5, 6$, and then high performance of the ESO can be promised. Figs. 3 and 4 show the time responses of the observer errors of P1 using the estimator in [19]. From the figures, we can see that the convergence time of Figs. 3 and 4 is slightly longer than Figs. 1 and 2. Using the estimator in [19], the errors converge to regions defined by $|\boldsymbol{e}_{1i}| < 1 \times 10^{-5}$, $|\boldsymbol{e}_{2i}| < 2 \times 10^{-4}(\mathrm{N}\cdot\mathrm{m}), i = 1, 2, 3$; $|\boldsymbol{e}_{1i}| < 5 \times 10^{-6}$, $|\boldsymbol{e}_{2i}| < 1 \times 10^{-4}(\mathrm{N}), i = 4, 5, 6$, which are larger than those obtained by the estimator shown in Figs. 1 and 2. Moreover, it can be seen that the steady-states depicted in Figs. 1 and 2 improve those of the estimator in Figs. 3 and 4 with a reduction in chattering.

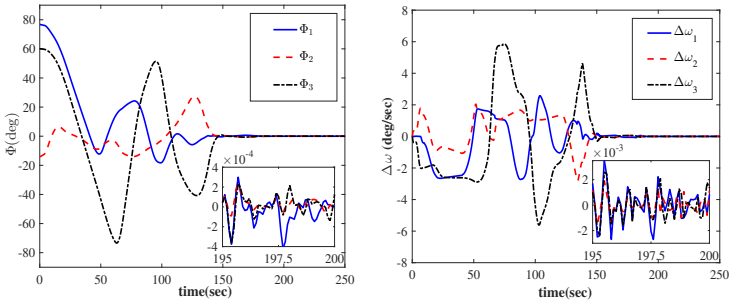

(a) (b)

Fig. 5: Time responses of attitude and angular velocity tracking errors (P1)

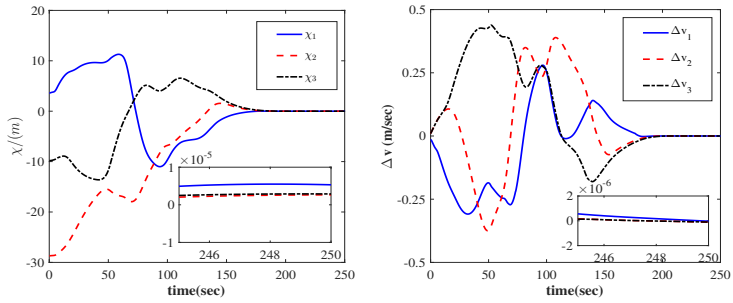

(a) (b)

Fig. 6: Time responses of position and translational velocity tracking errors (P1)

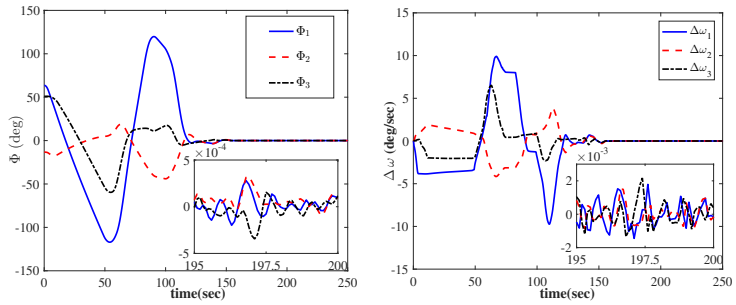

(a) (b)

Fig. 7: Time responses of attitude and angular velocity tracking errors (P2)

Fig. 5 shows the time responses of the rotational motion tracking errors of P1. It can be seen that the attitude of the virtual leader can be synchronized by the spacecraft with a settling time less than 180s, and the tracking errors are $|\boldsymbol{\Phi}_i| \leq 4 \times 10^{-4}(\mathrm{deg})$ and $|\Delta\boldsymbol{\omega}_i| \leq 2 \times 10^{-3}(\mathrm{deg/sec})$. The response curves of the translational motion tracking errors are depicted in Fig. 6. Observing the steady-state behavior, we find that the orbital tracking errors can converge to $|\boldsymbol{\chi}_i| \leq 1 \times 10^{-5}(\mathrm{m})$ and $|\Delta\boldsymbol{v}_i| \leq 2 \times 10^{-6}(\mathrm{m/sec})$ no more than 200s. The rotational motion and

translational motion tracking errors of P2 are shown in Figs. 7 and 8. From the figures, it can be deduced that the control performance is not effected by changes in the initial position within 100m of the origin.

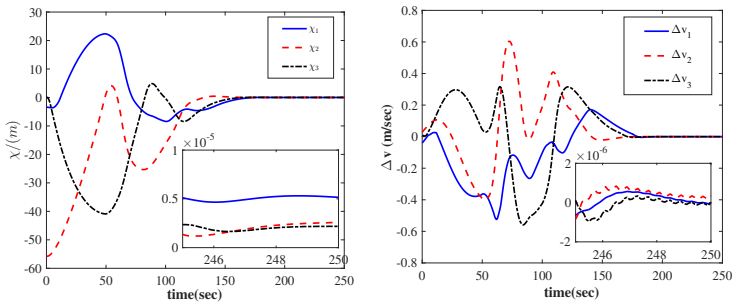

(a) (b)

Fig. 8: Time responses of position and translational velocity tracking errors (P2)

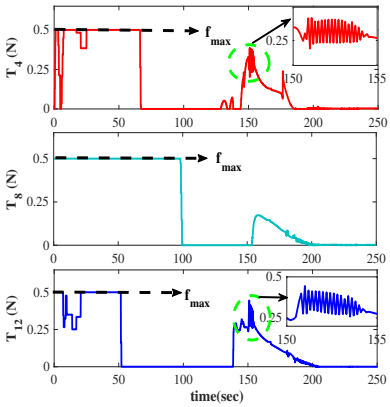

Fig. 9: Outputs of thrusters (P1)

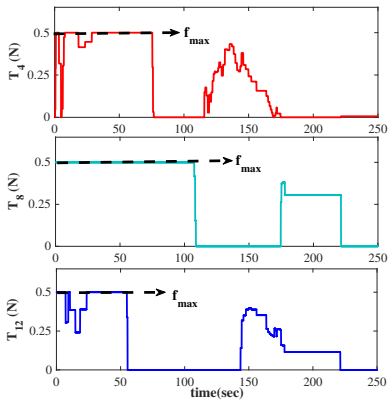

Fig. 10: Outputs of thrusters ($\gamma_1 = 0.1, \gamma_2 = 0.2$)

The outputs of the thrusters of P1 are presented in Fig. 9. For brevity, only the time responses of Thrusters 4, 8, 12 are shown. It can be seen that the control signal $\boldsymbol{\Gamma}_c$ is successfully allocated among the thrusters subject to the actuator saturation limits. The corresponding event-triggering release instants and inter-event times are shown in Fig. 11(a), where we can see that the Zeno phenomenon is avoided. In Fig. 9, the figures are magnified at some specific intervals, which are in accordance with the behaviors of the figures in Fig. 11(a). Moreover, the plots of Thrusters 4 and 12 change rapidly when $t \in [150, 155]$, because at this time $\boldsymbol{S}$ is close to origin, and t_k is mainly determined by γ_j. Smaller γ_j will lead to the rapid changes of the thruster actuations. This minimum change rate can be designed by increasing the magnitude of γ_j. Here, $\gamma_1 = 0.1, \gamma_2 = 0.2$ are used for comparison. From Figs. 10 and 11(b), we can see that in the time interval $t \in [150, 155]$, the control signal will be triggered only a limited number of times, and the communication burden is reduced. However, Fig. 12 shows that the control performance of P1 with lower γ_j is improved. These simulation results demonstrate the validity of the presentation in Remark 2, and a trade-off should be made between the communication burden and the control performance. Summarizing the above analysis of the simulation results, it can be concluded that with the aid of the finite-time ESO, the

proposed event-triggered adaptive controller can guarantee that the spacecraft tracking maneuver is achieved with high accuracy and Zeno behavior can be avoided.

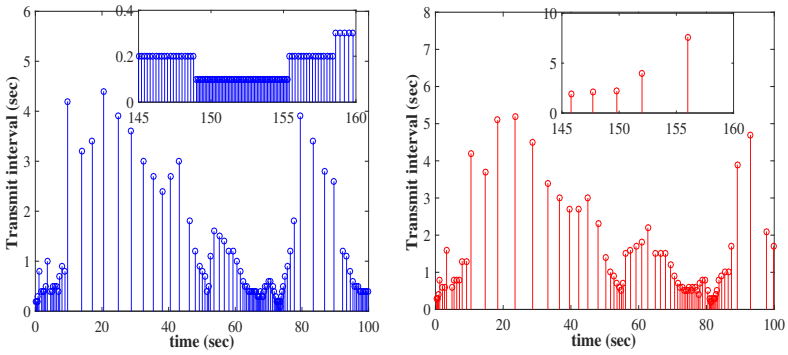

(a) (b)

Fig. 11: The event-triggering release instants and inter-event times: (a) P1; (b) $\gamma_1 = 0.1, \gamma_2 = 0.2$

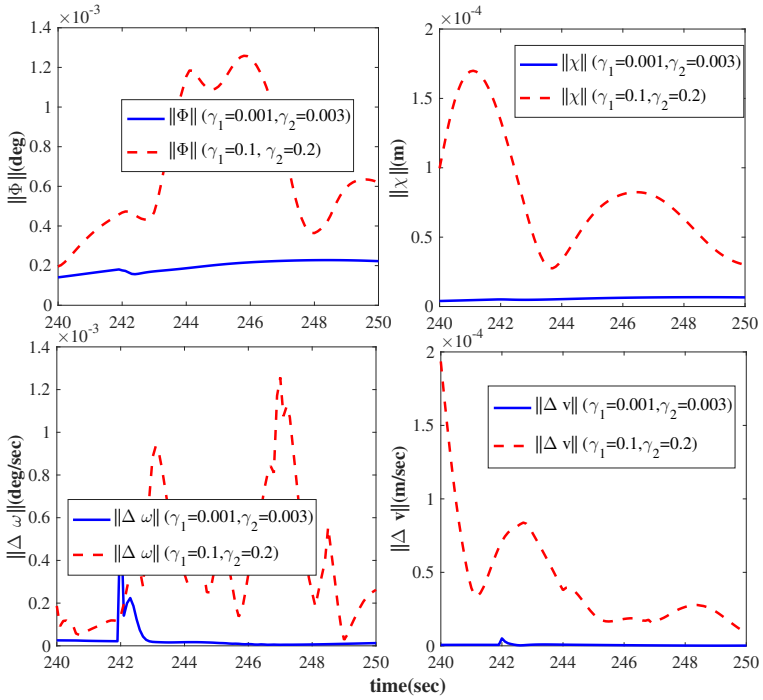

Fig. 12: Performance comparison between P1 and $\gamma_1 = 0.1, \gamma_2 = 0.2$

V. Conclusions

A dynamical synchronization control problem for a 6-DOF spacecraft with continuous low thrust propulsion was addressed in this paper. The key challenges met were to ensure high-accuracy tracking in the presence of internal and external disturbance torques and forces. Simultaneously, the on-board data transmission was reduced using an event-triggered control while maintaining system stability. Ultimately the inclusion on the embedding of the

event-triggered algorithm within the closed-loop system is able to reduce transmission requirement and thus reduce band-width requirement for the control system. In addition, one of the challenges of using finite-time extended state observers to develop controller is in the excessive tuning of the observer parameters. In this paper, a theoretical basis for tuning these parameters to guarantee convergence to a small bounded region of the desired state was established via Lyapunov theory. Moreover, the proposed event-triggering strategy significantly reduced the usage of the spacecraft communication channel and also guaranteed the Zeno free execution during the whole control process.

REFERENCES

[1] J. Wang, H. Liang, Z. Sun, S. Zhang, and M. Liu, "Finite-time control for spacecraft formation with dual-number-based description," *Journal of Guidance, Control, and Dynamics*, vol. 35, no. 3, pp. 950–962, 2012.

[2] D. Lee and G. Vukovich, "Adaptive finite-time control for spacecraft hovering over an asteroid," *IEEE Transactions on Aerospace and Electronic Systems*, vol. 52, no. 3, pp. 1183–1196, 2016.

[3] D. Lee, A. K. Sanyal, and E. A. Butcher, "Asymptotic tracking control for spacecraft formation flying with decentralized collision avoidance," *Journal of Guidance, Control, and Dynamics*, vol. 38, no. 4, pp. 587–600, 2014.

[4] H. Gui and G. Vukovich, "Dual-quaternion-based adaptive motion tracking of spacecraft with reduced control effort," *Nonlinear Dynamics*, vol. 83, no. 1-2, pp. 597–614, 2016.

[5] J. A. Starek, B. Açıkmeşe, I. A. Nesnas, and M. Pavone, "Spacecraft autonomy challenges for next-generation space missions," *Lecture Notes in Control and Information Sciences*, vol. 460, pp. 1–48, 2016.

[6] A. Dono, L. Plice, J. Mueting, T. Conn, and M. Ho, "Propulsion trade studies for spacecraft swarm mission design," in *IEEE Aerospace Conference*. Big Sky, MT, United States: IEEE Publications, 2018, pp. 1–12.

[7] A. Poghosyan and A. Golkar, "Cubesat evolution: analyzing cubesat capabilities for conducting science missions," *Progress in Aerospace Sciences*, vol. 88, pp. 59–83, 2017.

[8] H. C. Henninger and J. D. Biggs, "Near time-minimal earth to l1 transfers for low-thrust spacecraft," *Journal of Guidance, Control, and Dynamics*, vol. 40, no. 11, pp. 2999–3004, 2017.

[9] C. S. Arnot, C. R. McInnes, R. J. McKay, M. Macdonald, and J. D. Biggs, "Orbit period modulation for relative motion using continuous low thrust in the two-body and restricted three-body problems," *Celestial Mechanics and Dynamical Astronomy*, vol. 130, no. 12, pp. 1–23, 2018.

[10] R. McKay, M. Macdonald, J. Biggs, and C. McInnes, "Survey of highly-non-keplerian orbits with low-thrust propulsion," *Journal of Guidance, Control, and Dynamics*, vol. 34, no. 3, pp. 645–666, 2011.

[11] S. Segal, P. Gurfil, and K. Shahid, "In-orbit tracking of resident space objects: A comparison of monocular and stereoscopic vision," *IEEE Transactions on Aerospace and Electronic Systems*, vol. 50, no. 1, pp. 676–688, 2014.

[12] H. Gui and G. Vukovich, "Finite-time output-feedback position and attitude tracking of a rigid body," *Automatica*, vol. 74, pp. 270–278, 2016.

[13] N. Filipe, A. Valverde, and P. Tsiotras, "Pose tracking without linear and angular-velocity feedback using dual quaternions," *IEEE Transactions on Aerospace and Electronic Systems*, vol. 52, no. 1, pp. 411–422, 2016.

[14] L. Sun and W. Huo, "6-dof integrated adaptive backstepping control for spacecraft proximity operations," *IEEE Transactions on Aerospace and Electronic Systems*, vol. 51, no. 3, pp. 2433–2443, 2015.

[15] G. Fursht and M. Idan, "Experimental evaluation of sliding-mode controller for seeker-head line-of-sight stabilization," *Journal of Guidance, Control, and Dynamics*, vol. 39, no. 10, pp. 2434–2438, 2016.

[16] X. Shi, Z. Zhou, and D. Zhou, "Finite-time attitude trajectory tracking control of rigid spacecraft," *IEEE Transactions on Aerospace and Electronic Systems*, vol. 53, no. 6, pp. 2913–2923, 2017.

[17] Y. Bai, J. D. Biggs, F. B. Zazzera, and N. Cui, "Adaptive attitude tracking with active uncertainty rejection," *Journal of Guidance, Control, and Dynamics*, vol. 41, no. 2, pp. 546–554, 2018.

[18] L. Yin, Y. Xia, Z. Deng, and B. Huo, "Extended state observer-based attitude fault-tolerant control of rigid spacecraft," *International Journal of Systems Science*, vol. 49, no. 12, pp. 2525–2535, 2018.

[19] A.-M. Zou, A. H. de Ruiter, and K. D. Kumar, "Disturbance observer-based attitude control for spacecraft with input mrs," *IEEE Transactions on Aerospace and Electronic Systems*, vol. 55, no. 1, pp. 384–396, 2019.

[20] J. Zhang, D. Ye, Z. Sun, and C. Liu, "Extended state observer based robust adaptive control on se (3) for coupled spacecraft tracking maneuver with actuator saturation and misalignment," *Acta Astronautica*, vol. 143, pp. 221–233, 2018.

[21] Z. Zhao and B. Guo, "A novel extended state observer for output tracking of mimo systems with mismatched uncertainty," *IEEE Transactions on Automatic Control*, vol. 63, no. 1, pp. 211–218, 2018.

[22] C. Zhang, J. Wang, R. Sun, D. Zhang, and X. Shao, "Multi-spacecraft attitude cooperative control using model-based event-triggered methodology," *Advances in Space Research*, vol. 62, no. 9, pp. 2620–2630, 2018.

[23] C. Zhang, J. Wang, D. Zhang, and X. Shao, "Learning observer based and event-triggered control to spacecraft against actuator faults," *Aerospace Science and Technology*, vol. 78, pp. 522–530, 2018.

[24] B. Wu, Q. Shen, and X. Cao, "Event-triggered attitude control of spacecraft," *Advances in Space Research*, vol. 61, no. 3, pp. 927–934, 2018.

[25] X. Su, X. Liu, P. Shi, and Y. Song, "Sliding mode control of hybrid switched systems via an event-triggered mechanism," *Automatica*, vol. 90, pp. 294–303, 2018.

[26] L. Xing, C. Wen, Z. Liu, H. Su, and J. Cai, "Event-triggered adaptive control for a class of uncertain nonlinear systems," *IEEE Transactions on Automatic Control*, vol. 62, no. 4, pp. 2071–2076, 2017.

[27] X. Zhang, Q. Han, and B. Zhang, "An overview and deep investigation on sampled-data-based event-triggered control and filtering for networked systems," *IEEE Transactions on Industrial Informatics*, vol. 13, no. 1, pp. 4–16, 2017.

[28] S. Zheng, P. Shi, S. Wang, and Y. Shi, "Event triggered adaptive fuzzy consensus for interconnected switched multi-agent systems," *IEEE Transactions on Fuzzy Systems*, vol. 27, no. 1, pp. 144–158, 2019.

[29] P. Shi, H. Wang, and C. Lim, "Network-based event-triggered control for singular systems with quantizations," *IEEE Transactions on Industrial Electronics*, vol. 63, no. 2, pp. 1230–1238, 2016.

[30] J. Zhang, D. Ye, J. D. Biggs, and Z. Sun, "Finite-time relative orbit-attitude tracking control for multi-spacecraft with collision avoidance and changing network topologies," *Advances in Space Research*, vol. 63, no. 3, pp. 1161–1175, 2019.

[31] J. D. Biggs and L. Colley, "Geometric attitude motion planning for spacecraft with pointing and actuator constraints," *Journal of Guidance, Control, and Dynamics*, vol. 39, no. 7, pp. 1672–1677, 2016.

[32] D. H. S. Maithripala, W. P. Dayawansa, and J. M. Berg, "Intrinsic observer-based stabilization for simple mechanical systems on lie groups," *SIAM Journal on Control and Optimization*, vol. 44, no. 5, pp. 1691–1711, 2005.

[33] D. Ye, J. Zhang, and Z. Sun, "Extended state observer–based finite-time controller design for coupled spacecraft formation with actuator saturation," *Advances in Mechanical Engineering*, vol. 9, no. 4, p. 1687814017696413, 2017.

[34] B. Xiao, S. Yin, and L. Wu, "A structure simple controller for satellite attitude tracking maneuver," *IEEE Transactions on Industrial Electronics*, vol. 64, no. 2, pp. 1436–1446, 2017.

[35] H. Gui and A. H. de Ruiter, "Adaptive fault-tolerant spacecraft pose tracking with control allocation," *IEEE Transactions on Control Systems Technology*, no. 99, pp. 1–16, 2017.

[36] F. Curti, M. Romano, and R. Bevilacqua, "Lyapunov-based thrusters' selection for spacecraft control: Analysis and experimentation," *Journal of Guidance, Control, and Dynamics*, vol. 33, no. 4, pp. 1143–1160, 2010.

[37] X. Huang, Y. Yan, Y. Zhou, and Y. Yang, "Dual-quaternion based distributed coordination control of six-dof spacecraft formation with collision avoidance," *Aerospace Science and Technology*, vol. 67, pp. 443–455, 2017.